Draft version December 31, 2021
Typeset using LaTeX **twocolumn** style in AASTeX62

XMM-Newton detection and spectrum of the second fastest spinning pulsar PSR J0952−0607

Wynn C.G. Ho,[1,2] Craig O. Heinke,[3] and Andrey I. Chugunov[4]

[1] *Department of Physics and Astronomy, Haverford College, 370 Lancaster Avenue, Haverford, PA 19041, USA*
[2] *Mathematical Sciences, Physics and Astronomy, and STAG Research Centre, University of Southampton, Southampton SO17 1BJ, United Kingdom*
[3] *Department of Physics, University of Alberta, CCIS 4-183, Edmonton, AB T6G 2E1, Canada*
[4] *Ioffe Institute, 26 Politekhnicheskaya, St Petersburg 194021, Russia*

(Received 2019 May 28; Revised 2019 July 19; Accepted 2019 July 23)

Submitted to ApJ

ABSTRACT

With a spin frequency of 707 Hz, PSR J0952−0607 is the second fastest spinning pulsar known. It was discovered in radio by LOFAR in 2017 at an estimated distance of either 0.97 or 1.74 kpc and has a low-mass companion with a 6.42 hr orbital period. We report discovery of the X-ray counterpart of PSR J0952−0607 using *XMM-Newton*. The X-ray spectra can be well-fit by a single power law model ($\Gamma \approx 2.5$) or by a thermal plus power law model ($kT_{\rm eff} \approx 40$ eV and $\Gamma \approx 1.4$). We do not detect evidence of variability, such as that due to orbital modulation from pulsar wind and companion star interaction. Because of its fast spin rate, PSR J0952−0607 is a crucial source for understanding the r-mode instability, which can be an effective mechanism for producing gravitational waves. Using the high end of our measured surface temperature, we infer a neutron star core temperature of $\sim 10^7$ K, which places PSR J0952−0607 within the window for the r-mode to be unstable unless an effect such as superfluid mutual friction damps the fluid oscillation. The measured luminosity limits the dimensionless r-mode amplitude to be less than $\sim 1 \times 10^{-9}$.

Keywords: gravitational waves — pulsars: general — pulsars: individual (PSR J0952−0607) — stars: neutron — X-rays: stars

1. INTRODUCTION

Despite sensitivity to and searches for pulsars with even higher spin rates, the fastest pulsars known to date among non-accreting pulsars are PSR J1748−2446ad (with a spin rate $\nu_{\rm s} = 716$ Hz; Hessels et al. 2006), PSR J0952−0607 ($\nu_{\rm s} = 707$ Hz; Bassa et al. 2017), and PSR B1937+21 ($\nu_{\rm s} = 642$ Hz; Backer et al. 1982) and among accreting pulsars are 4U 1608−52 ($\nu_{\rm s} = 620$ Hz), SAX J1750.8−2900 ($\nu_{\rm s} = 601$ Hz), and IGR 00291+5934 ($\nu_{\rm s} = 599$ Hz). The observed spin rates are well below the theoretical limit of ∼2000 Hz (Cook et al. 1994; Haensel et al. 1999). This suggests a mechanism which prevents fast rotation (Chakrabarty et al. 2003; Chakrabarty 2008; Papitto et al. 2014; Patruno et al. 2017; Gittins & Andersson 2019), such as mechanisms associated with gravitational wave emission since their torques depend strongly on spin rate.

One particular mechanism that is of great interest is that associated with the r-mode fluid oscillation, because it can be a strong source of gravitational waves (Andersson 1998; Friedman & Morsink 1998)) via the Chandrasekhar-Friedman-Schutz (CFS) instability (Chandrasekhar 1970; Friedman & Schutz 1978; see also Chugunov 2017). The strength of the r-mode instability is characterized by the balance between the timescale of mode growth by gravitational wave emission $t_{\rm gw}$ (which depends strongly on spin frequency, i.e., $t_{\rm gw} \propto \nu_{\rm s}^{-6}$) and timescale of viscous damping (which is temperature-dependent; e.g., $t_{\rm visc} \propto T^2$; Andersson & Kokkotas 2001). However, our theoretical picture of r-modes is severely problematic (see, e.g., Ho et al. 2011; Haskell et al. 2012; Chugunov et al. 2017). Thus it is vital to identify fast and hot neutron

Corresponding author: Wynn Ho
wynnho@slac.stanford.edu

stars which can be used to better understand the nature of the r-mode mechanism. Here we report the X-ray detection of the second fastest pulsar, PSR J0952−0607, which provides possibly the strongest r-mode constraints for millisecond pulsars.

PSR J0952−0607 was discovered at radio frequencies using LOFAR during a targeted search of gamma-ray sources detected by *Fermi* but not associated with other known sources (Bassa et al. 2017). Optical observations identify the binary companion of the pulsar, and the companion star's low mass and short 6.42 hr orbital period suggest PSR J0952−0607 is in a black widow system, where the pulsar wind irradiates and evaporates the companion star. The position of PSR J0952−0607 used for radio timing is that determined from its optical counterpart, i.e., (R.A.,decl.[J2000]) = ($09^{\rm h}52^{\rm m}08\overset{\rm s}{.}319$,$-06°07'23\overset{''}{.}49$). The distance is determined from the measured dispersion measure (DM = 22.4 pc cm^{-3}) and found to be either d = 0.97 kpc or 1.74 kpc, depending on which model of Galactic electron distribution is used (NE2001 or YMW16, respectively). Henceforth we assume a distance of 1.74 kpc, unless otherwise noted. Bassa et al. (2017) estimate an interstellar absorption column $N_{\rm H} = 4 \times 10^{20}$ cm^{-2} from a Galactic extinction model and distance, which agrees with $N_{\rm H} = 3.9 \times 10^{20}$ cm^{-2} estimated from HI in the direction of PSR J0952−0607 (Dickey & Lockman 1990). We estimate a somewhat larger $N_{\rm H} = 6.7^{+2.9}_{-2.0} \times 10^{20}$ cm^{-2} (90% confidence level) using the empirical relation between $N_{\rm H}$ and DM from He et al. (2013). Since PSR J0952−0607 is in a short orbital period black widow system, a higher $N_{\rm H}$ could be measured, e.g., as might be possible using dispersion measure variations during radio eclipses such as that reported by Main et al. (2018) for PSR B1957+20. Using a short 4.6 ks exposure with *Swift* XRT, Bassa et al. (2017) obtain a 3σ upper limit on the 0.3–10 keV flux $f_{0.3-10} < 1.1 \times 10^{-13}$ erg cm^{-2} s^{-1}, which corresponds to a X-ray luminosity limit of $L < 1.1 \times 10^{31}$ erg s^{-1} at 0.97 kpc or 3.6×10^{31} erg s^{-1} at 1.74 kpc.

In Section 2, we describe the *XMM-Newton* observation of PSR J0952−0607 and our procedure for processing the data. Section 3 and 4 give details of our spectral fitting and variability search analyses. In Section 5, we summarize and discuss our results and use them to place constraints on the r-mode instability.

2. *XMM-Newton* OBSERVATIONS

XMM-Newton observed PSR J0952−0607 on 2018 May 4 (ObsID 0821520101) for 71.2 ks with EPIC in full frame imaging mode and using the thin optical filter. Figure 1 shows the MOS2 and pn images of the field around PSR J0952−0607. We process this data using SAS 17.0.0 (Gabriel et al. 2004) and CIAO 4.11 (Fruscione et al. 2006). Standard filtering is applied to both MOS and pn data, i.e., up to quadruple events are retained and energy ranges of 0.2–12 keV for MOS and 0.2–15 keV for pn are considered. To remove periods of background flaring, we apply count-rate cuts of 2.1, 3, and 18 s^{-1} and obtain effective exposure times of 58.5, 63.3, and 44.0 ks for MOS1, MOS2, and pn, respectively. We then use `wavdetect` on the pn data to determine the source position and its uncertainty to be (R.A.,decl.[J2000]) = ($09^{\rm h}52^{\rm m}08\overset{\rm s}{.}27 \pm 0.03$, $-06°07'27\overset{''}{.}80 \pm 0.45$); all errors are 1$\sigma$ unless otherwise noted. With an angular resolution of 4.″1 for pn and estimated systematic uncertainty[1] in *XMM-Newton* positions of 1.″2 (1σ), we can positively associate our X-ray

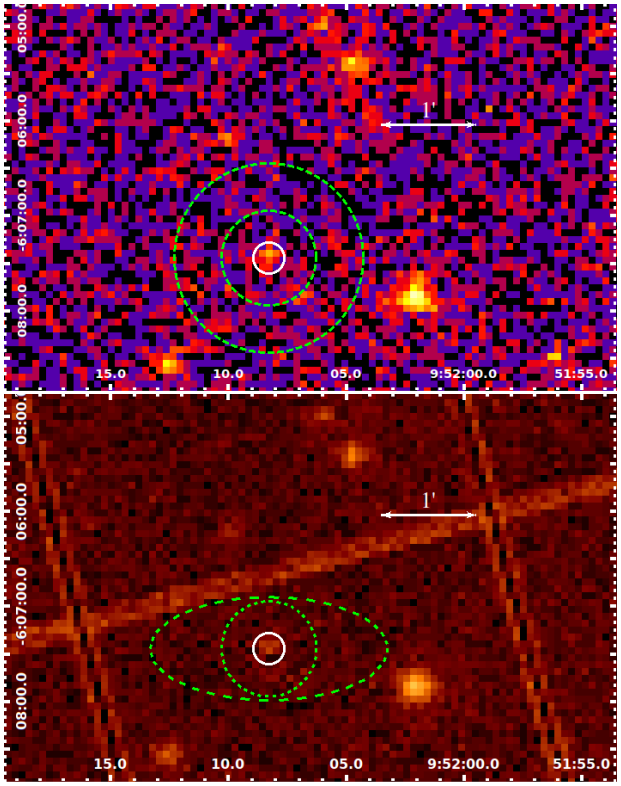

Figure 1. MOS2 (top) and pn (bottom) images of the field of PSR J0952−0607. North is up, and east is left. In both images, the inner solid circle (of radius 10″) is used for source spectral extraction. In the MOS2 image, the dashed annulus (of inner and outer radii 30″ and 60″, respectively) is used for background spectral extraction (similarly for MOS1 data), while in the pn image, the ellipsoidal dashed annulus (of circular inner radius 30″ and maximum outer radius 75″) is used for background spectral extraction.

[1] http://xmm2.esac.esa.int/docs/documents/CAL-TN-0018.pdf

point source with that of PSR J0952−0607. We generate psf images of the MOS1, MOS2, and pn data using `psfgen`, centered on the source position at 0.5, 1, and 3 keV, and do not find any noticeable extended emission.

We use `eregionanalyse` to determine optimum regions for extracting MOS and pn source spectra. With background regions shown in Figure 1, this procedure indicated an optimal extraction radius of 10″ and background-subtracted counts of 39 ± 10, 65 ± 12, and 142 ± 20 and count-rates of $(0.67 \pm 0.18) \times 10^{-3}$, $(1.02 \pm 0.19) \times 10^{-3}$, and $(3.24 \pm 0.44) \times 10^{-3}$ s^{-1} for MOS1, MOS2, and pn, respectively. Using `epatplot`, we find our spectra of PSR J0952−0607 are not affected by pile-up. We account for bad pixels and chip gaps using `backscale`. We then compute rmf and arf files. In order to improve statistics, we combine the MOS1 and MOS2 spectra using `epicspeccombine`. Spectra are binned using ftools task `grppha` to a minimum of 15 photons per bin for each of the combined MOS spectrum and pn spectrum.

We perform spectral fitting using Xspec 12.10.1 (Arnaud 1996). We use `constant` to model a possible instrumental difference between MOS and pn spectral normalizations, and we fix its value to 1 for the pn spectrum and allow it to vary for the combined MOS spectrum. To model X-ray absorption by the interstellar medium, we use `tbabs` with abundances from Wilms et al. (2000). To model the intrinsic spectrum of PSR J0952−0607, we consider either a single component composed of a power law (PL; `powerlaw`), blackbody (BB; `bbodyrad`), or neutron star atmosphere, or two components composed of combinations of the above. For a (non-magnetic) neutron star hydrogen atmosphere model X-ray spectrum, we use `nsatmos` (Heinke et al. 2006) and fix the model parameters of neutron star mass and radius to $M = 1.4\,M_{\rm Sun}$ and $R = 10$ km, respectively, and distance to $d = 1.74$ kpc. We also consider the non-magnetic atmosphere model `nsspec` with an iron or solar composition, which are computed for fixed $M = 1.4\,M_{\rm Sun}$ and $R = 10$ km and thus fixed surface gravity and gravitational redshift (Gänsicke et al. 2002).

3. SPECTRAL ANALYSIS

For our first set of spectral fits, we allow the absorption parameter $N_{\rm H}$ to be free to vary. The results of our simultaneous fit of the pn and combined MOS spectra are given in Table 1. The top panel of Figure 2 shows the results of a spectral fit using a `powerlaw` model. A power law provides a generally good fit of the spectra of PSR J0952−0607, with a photon index $\Gamma \approx 2.5^{+0.5}_{-0.4}$ and unabsorbed 0.3–10 keV flux $f^{\rm unabs}_{0.3-10} \approx 9 \times 10^{-15}$ erg cm^{-2} s^{-1}. The latter results in a luminosity $L = 3 \times 10^{30}$ erg s^{-1} at a distance of 1.74 kpc, which is more than ten times lower than the

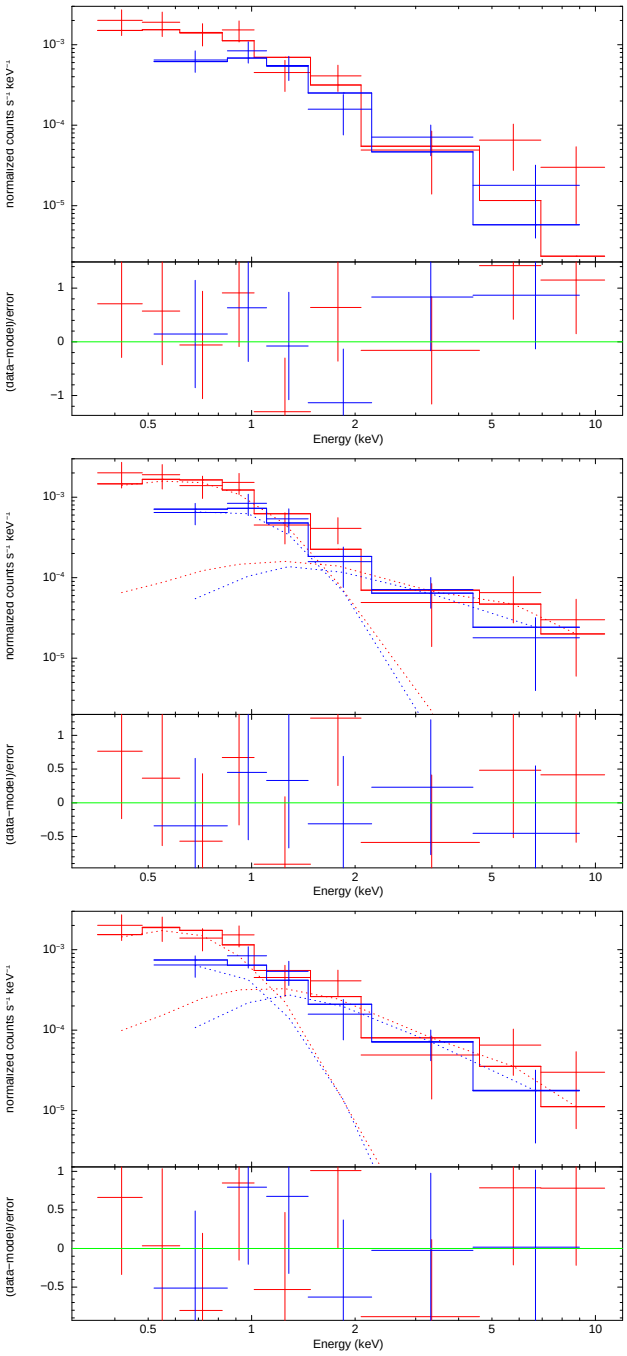

Figure 2. EPIC-pn (red) and combined MOS1 and MOS2 (blue) spectra (upper panels) and model fit residuals (lower panels). Solid lines are model fits, either `powerlaw` (top), `nsatmos+powerlaw` (middle), and `nsatmos+powerlaw` with fixed `nsatmos` normalization = 1 (bottom). For two component models, dotted lines show individual components, i.e, `nsatmos` at low energies and `powerlaw` at high energies.

Table 1. Spectral model fits which allow for a varying $N_{\rm H}$

Model fit parameter	PL	BB	BB+PL	NSATMOS+PL	NSATMOS+PL	2BB
$N_{\rm H}$ (10^{20} cm^{-2})	$12.2^{+7.2}_{-4.8}$	$2.6^{+4.4}_{-2.2}$	$7.6^{+11}_{-5.1}$	11^{+15}_{-7}	$28.7^{+8.3}_{-7.8}$	$5.2^{+6.8}_{-3.6}$
kT_∞ or $kT_{\rm eff}$ (eV)		238^{+36}_{-33}	175^{+44}_{-50}	84^{+44}_{-41}	38^{+2}_{-4}	200^{+35}_{-33}
R_∞ or $R_{\rm em}$ (m) [a]		58^{+25}_{-17}	110^{+180}_{-46}	800^{+5000}_{-500}	fixed 10^4	84^{+56}_{-28}
$kT_\infty^{\rm hot}$ (eV)						1900^{+2400}_{-800}
$R_\infty^{\rm hot}$ (m)						$1.3^{+1.0}_{-0.2}$
Γ	$2.51^{+0.53}_{-0.39}$		0.78 ± 0.85	0.59 ± 0.90	$1.38^{+0.64}_{-0.61}$	
PL normalization (10^{-6})	$1.74^{+0.46}_{-0.35}$		$0.34^{+0.37}_{-0.25}$	$0.26^{+0.56}_{-0.18}$	$0.76^{+0.56}_{-0.39}$	
MOS-pn normalization	$1.23^{+0.27}_{-0.23}$	$1.31^{+0.31}_{-0.25}$	$1.25^{+0.27}_{-0.22}$	$1.24^{+0.27}_{-0.22}$	$1.22^{+0.26}_{-0.22}$	$1.27^{+0.28}_{-0.23}$
$f^{\rm abs}_{0.3-1}$ (10^{-15} erg cm^{-2} s^{-1})	1.9	1.9	2.0	2.0	2.1	2.0
$f^{\rm abs}_{1-10}$ (10^{-15} erg cm^{-2} s^{-1})	3.6	1.3	7.6	8.0	6.3	7.1
$f^{\rm abs}_{0.3-10}$ (10^{-15} erg cm^{-2} s^{-1})	5.5	3.2	9.6	10.0	8.3	9.1
χ^2/dof	10.74/13	20.46/13	5.97/11	5.57/11	6.87/12	6.79/11

[a] Assuming $d = 1.74$ kpc to calculate R_∞ and $R_\infty^{\rm hot}$ and $R = 10$ km to calculate $R_{\rm em}$.

NOTE—Xspec models: PL=`powerlaw` and BB=`bbodyrad`. For NSATMOS, $d = 1.74$ kpc, $M = 1.4 M_{\rm Sun}$, and $R = 10$ km are assumed. All error bars are 1σ.

upper limits determined using a short *Swift* exposure by Bassa et al. (2017). Even though a power law is a good fit to the data, there is possibly unmodeled excess flux at the highest energies ($E \gtrsim 5$ keV), the derived $N_{\rm H} \approx (12^{+7}_{-5}) \times 10^{20}$ cm^{-2} is somewhat higher than the $(4-7) \times 10^{20}$ cm^{-2} estimated to be in the direction of PSR J0952−0607 (see Section 1), and the photon index $\Gamma \approx 2.5$ is relatively soft and suggestive that a thermal model is possibly more appropriate. However, single component thermal models are a poor fit: blackbody with χ^2/dof = 20/13 (see Table 1), `nsatmos` with χ^2/dof = 18/13, and `nsspec` with χ^2/dof = 23/13 for iron and χ^2/dof = 16/13 for solar composition. The poor fits are due to the model spectra not being able to match the observed flux at high energies ($\gtrsim 2$ keV). Note that, for the spectral fit using `nsatmos`, we allow the model normalization to vary, and the fit results yield values smaller than 1; while this is formally allowed and can be interpreted as emission from only a fraction of the stellar surface, it is not strictly correct since the model is computed assuming emission from the entire surface. If the normalization is fixed at one, then a much larger distance would have to be assumed (for the same inferred flux and temperature).

Two component spectral models produce improved fits because a thermal component can reproduce the low energy spectrum and a power law or second hot blackbody reproduces the high energy emission, even above 5 keV (see Figure 2). In the cases of BB+PL and 2BB, the derived $N_{\rm H}$ (albeit with large uncertainty) matches that inferred from the DM of PSR J0952−0607. However the resulting fit parameters are somewhat unusual ($\Gamma \sim 0.8$ or $R_\infty^{\rm hot} = 1$ m), and the two component model fits are not strongly preferred (f-test of BB+PL compared to PL yields a probability of 4.0% of producing by chance such a fit improvement when adding a blackbody). A model fit using NSATMOS+PL with the normalization of `nsatmos` free to vary (see above) gives results that are comparable to those of BB+PL. On the other hand, if we fix this model normalization to be unity, such that $R_{\rm em} = R = 10$ km, then the surface temperature $T_{\rm eff} = 4.4^{+0.5}_{-1.0} \times 10^5$ K (at 90% confidence), and power law index $\Gamma \approx 1.4$ is similar to that seen in other pulsars (see, e.g., De Luca et al. 2005; Guillot et al. 2016, where $\Gamma = 1.5-2.1$ is found for four pulsars), but $N_{\rm H} = (2.9 \pm 0.8) \times 10^{21}$ cm^{-2} is much greater that expected. In this last case, a high $N_{\rm H}$ is needed to strongly reduce the low energy model flux, which is high because the `nsatmos` normalization is not allowed to be smaller and emission is from the entire neutron star surface. Similar results are obtained using `nsatmos+nsatmos`, where one component has a normalization fixed at one to model emission from the entire surface while the other component with a variable normalization could be that due to a hot spot. Also problematic with this model fit is that the temperature of the hot component hits the upper limit of the model ($\log T_{\rm eff} = 6.5$); since the ratio of blackbody to atmosphere temperatures is seen to be ~ 2 in spectral studies of other neutron stars, we expect this hot component to have a temperature that exceeds 10^7 K. A f-test of NSATMOS+PL with fixed `nsatmos` normalization compared to PL yields a probability of 2.3%.

Table 2. Spectral model fits with fixed $N_{\rm H}$ and NSATMOS normalization (= 1)

Model fit parameter	PL	NSATMOS+PL	PL	NSATMOS+PL
fixed $N_{\rm H}$ (10^{20} cm^{-2})	4	4	10	10
$kT_{\rm eff}$ (eV)		< 18		< 27
Γ	1.85 ± 0.15	1.85 ± 0.14	2.36 ± 0.19	$2.36^{+0.19}_{-0.25}$
PL normalization (10^{-6})	1.22 ± 0.17	1.22 ± 0.17	1.62 ± 0.22	$1.62^{+0.20}_{-0.22}$
MOS-pn normalization	$1.27^{+0.30}_{-0.24}$	$1.27^{+0.29}_{-0.23}$	$1.23^{+0.27}_{-0.23}$	$1.23^{+0.27}_{-0.22}$
$f^{\rm abs}_{0.3-1}$ (10^{-15} erg cm^{-2} s^{-1})	1.6	1.6	1.9	1.9
$f^{\rm abs}_{1-10}$ (10^{-15} erg cm^{-2} s^{-1})	5.3	5.3	3.9	3.9
$f^{\rm abs}_{0.3-10}$ (10^{-15} erg cm^{-2} s^{-1})	6.9	6.9	5.8	5.8
χ^2/dof	15.34/14	15.35/13	10.92/14	10.92/13

NOTE—Xspec model: PL=`powerlaw`. For NSATMOS, $d = 1.74$ kpc, $M = 1.4 M_{\rm Sun}$, and $R = 10$ km are assumed. All error bars are 1σ, except for 90% confidence level upper limit on $kT_{\rm eff}$.

In summary, while several models can fit well the spectrum of PSR J0952−0607, none are entirely satisfactory because either the inferred $N_{\rm H}$ is too high or Γ is too low or too high. Nevertheless, to obtain further constraints on the surface temperature of PSR J0952−0607, we perform spectral fits using the NSATMOS+PL model with `nsatmos` normalization fixed at 1 and absorption column fixed at either $N_{\rm H} = 4 \times 10^{20}$ or 1×10^{21} cm^{-2}, i.e., values that span the likely range of $N_{\rm H}$ (see Section 1). At these low $N_{\rm H}$ values compared to much higher values preferred when $N_{\rm H}$ is free to vary, the thermal component is forced to have a low temperature (since the emission region is the entire stellar surface), and the model fit is essentially that of a single component power law (see Table 2). From these spectral fits, we derive upper limits (at 90% confidence) on the surface temperature of 2.1×10^5 and 3.1×10^5 K for $N_{\rm H} = 4 \times 10^{20}$ and 1×10^{21} cm^{-2}, respectively. Identical temperature limits are obtained when using non-magnetic, fully-ionized helium atmosphere model spectra (Ho & Lai 2001). In order to obtain a surface temperature measurement, as opposed to an upper limit, one needs $N_{\rm H} \gtrsim 1.2 \times 10^{21}$ cm^{-2}.

4. VARIABILITY ANALYSIS

With a small inferred size of the X-ray emitting region, such as that of a hot spot on the neutron star surface, there is the possibility of detectable X-ray pulsations if the viewing geometry is favorable and pulsations have a high enough amplitude. Unfortunately, since the time resolution of our full frame imaging mode observations is 2.6 s for MOS and 73.4 ms for pn, we are unable to search for variability due to the pulsar spin period of 1.41 ms. Nevertheless, we still perform an analysis to determine if there are other periodic signals in the data. We consider MOS2 and pn independently. We first apply a barycentric correction using `barycen` and DE405 ephemeris, then extract source and background 0.3–5 keV light curves using the same spatial regions as in the spectral analysis, and obtain corrected light curves using `epiclccorr`. The resulting light curves of PSR J0952−0607 with a bin size of 5000 s for MOS2 data and 3000 s for pn data do not show clear evidence of variability at the 6.42 hr orbital period; note that our pn and MOS exposure times span 2 and 2.5 orbital cycles, respectively. Smaller bin sizes result in time intervals where the count-rate is zero. We also do not find variability using `glvary`, with a variability index of 0.

5. DISCUSSION

In this work, we analyze a recent *XMM-Newton* observation of the second fastest pulsar known and report on our detection of its X-ray counterpart. The data are sufficient for extraction of source spectra, and we find that these spectra can be fit well by a single power law model or a two component thermal plus power law model. We do not detect any significant variability of the source, although the *XMM-Newton* full frame imaging observations do not allow us to search for variations on the timescale of the short spin period of PSR J0952−0607.

With gamma-ray flux $f_\gamma = 2.6 \times 10^{-12}$ erg cm^{-2} s^{-1}, spin period $P = 1.41$ ms, and spin period time derivative $\dot{P} = 4.6 \times 10^{-21}$ s s^{-1} (Nieder et al. 2019), PSR J0952−0607 has $f_\gamma / f^{\rm unabs}_{0.3-10} \approx 300$, spin-down energy loss rate $\dot{E} = 6.4 \times 10^{34}$ erg s^{-1}, and $L/\dot{E} \approx 5 \times 10^{-5}$. The gamma-ray to X-ray flux ratio is typical for black widow pulsars (see, e.g., Marelli et al. 2015; Salvetti et al. 2017). The $L/\dot{E}$ is well below $\sim 10^{-3}$ seen in canonical rotation-powered pulsars (Becker 2009) but similar to those seen in several millisecond pulsars in the Galactic field (see, e.g., Kargaltsev et al. 2012; Lee et al. 2018) and globular clusters (Forestell et al.

2014; Bhattacharya et al. 2017). The spin-down rate of PSR J0952−0607 could be sufficient to power its thermal X-ray luminosity. For example, deviations from beta equilibrium in the core (via rotochemical heating) of PSR J0952−0607 produce a luminosity $\sim 5 \times 10^{31}$ erg s^{-1}, but this depends on uncertain properties of neutron superfluidity and proton superconductivity (Reisenegger 1995; Petrovich & Reisenegger 2010). Meanwhile, thermal creep of superfluid vortices dissipates energy at a rate of $\sim (0.02 - 2) \times 10^{30}$ erg s^{-1} in PSR J0952−0607 (Alpar et al. 1984a,b), and rotation-induced nuclear burning in the crust generates a heating rate of $\sim 5 \times 10^{29}$ erg s^{-1} in PSR J0952−0607 (Gusakov et al. 2015).

In Section 3, we use model fits of the *XMM-Newton* spectrum of PSR J0952−0607 to constrain its surface temperature, which in turn can be used to place limits on the neutron star core temperature T_c through well-studied $T_{\rm eff}$-T_c relations (see, e.g., Potekhin et al. 2015). For example, if the neutron star envelope is composed of iron, then

$$T_c({\rm Fe}) = 1.29 \times 10^8 \text{ K} \left[g_{14}^{-1} \left(\frac{T_{\rm eff}}{10^6 \text{ K}} \right)^4 \right]^{5/11}, \quad (1)$$

where $g \equiv 10^{14} g_{14}$ cm s^{-2} is surface gravity (Gudmundsson et al. 1982; Potekhin et al. 1997). On the other hand, for a fully accreted hydrogen envelope,

$$T_c({\rm H}) = 0.552 \times 10^8 \text{ K} \left[g_{14}^{-1} \left(\frac{T_{\rm eff}}{10^6 \text{ K}} \right)^4 \right]^{7/17} \quad (2)$$

(Potekhin et al. 1997). Using equations (1) and (2), our surface temperature measurement of $T_{\rm eff} \approx 4.4 \times 10^5$ K (for varying $N_{\rm H}$ and thermal plus power law model spectrum) yields a core temperature of $T_c = 1.9 \times 10^7$ K for an iron envelope or $T_c = 1.0 \times 10^7$ K for a hydrogen envelope. Meanwhile, our surface temperature upper limit of $T_{\rm eff} < 3.1 \times 10^5$ K (for fixed $N_{\rm H} = 1 \times 10^{21}$ cm^{-2} and simple power law model spectrum) yields core temperatures of $T_c < 1.0 \times 10^7$ K for an iron envelope or $T_c < 0.56 \times 10^7$ K for a hydrogen envelope.

As noted in Section 1, the r-mode instability is caused by growth of the oscillation mode through emission of gravitational waves and occurs on a timescale

$$t_{\rm gw} = 47 \text{ s} \left(\frac{1000 \text{ Hz}}{\nu_s} \right)^6, \quad (3)$$

while the oscillation is damped by viscosity on a timescale $t_{\rm visc}$, which in the simplest model is due to electron-electron scattering (once the core temperature drops below the neutron superfluid transition temperature) with

$$t_{\rm visc} = 2.2 \times 10^5 \text{ s} \left(\frac{T_c}{10^8 \text{ K}} \right)^2 \quad (4)$$

(Andersson & Kokkotas 2001; Shternin & Yakovlev 2008; Gusakov et al. 2014). Therefore the r-mode is unstable and grows when $t_{\rm gw} < t_{\rm visc}$ and is damped when $t_{\rm gw} > t_{\rm visc}$. This is illustrated in Figure 3, which displays the "r-mode instability window" based on the two primary parameters, ν_s and T_c, that determine $t_{\rm gw}$ and $t_{\rm visc}$; note that the dominant viscosity at $T_c \gtrsim 10^{10}$ K is not that given by equation (4) but by bulk viscosity. Also shown are (ν_s,T_c) for neutron stars in systems where these values or their limits can be determined (see Gusakov et al. 2014; Bhattacharya et al. 2017; Mahmoodifar & Strohmayer 2017; Rangelov et al. 2017; Schwenzer et al. 2017; Gonzalez-Caniulef et al. 2019, and references therein; see also Mahmoodifar & Strohmayer 2013; for simplicity, we plot fiducial T_c from Gusakov et al. 2014, but we note there is factor of $\lesssim 3$ uncertainty due to uncertain envelope composition and gravitational redshift). For PSR J0952−0607, we show two values of T_c derived from our spectral fits using either a varying or fixed $N_{\rm H}$ and assuming a fully accreted hydrogen envelope.

Our results for PSR J0952−0607 can be used to inform our understanding of r-modes. Figure 3 shows that many neutron stars, including PSR J0952−0607 (see below), should be unstable to r-mode growth and thus are potentially strong sources of gravitational waves. This in part motivates r-mode searches by LIGO/Virgo (Abbott et al. 2017; Meadors et al. 2017; Abbott et al. 2019a; Caride et al. 2019). However, spin and thermal evolution calculations indicate neutron stars should only spend a short time within the instability window and long time outside the window (Levin 1999; Heyl 2002). Thus one expects few sources to lie within the window at any one time compared to the number of sources outside the window, contrary to what is shown in Figure 3. This suggests that the instability window should be much smaller and our theoretical understanding of the physics that determines $t_{\rm visc}$ (e.g., neutrino emission, crust elasticity, superfluidity, and/or existence of hyperonic or quark matter; Andersson & Kokkotas 2001; Alford et al. 2012b,a) is inadequate (Ho et al. 2011; Haskell et al. 2012; Chugunov et al. 2017). For example, one possible mechanism that could close the window at $T_c < 10^9$ K is superfluid mutual friction, i.e., dissipation due to interactions between protons/electrons and superfluid neutron vortices (Haskell et al. 2009). Its possible effect on the r-mode instability window is

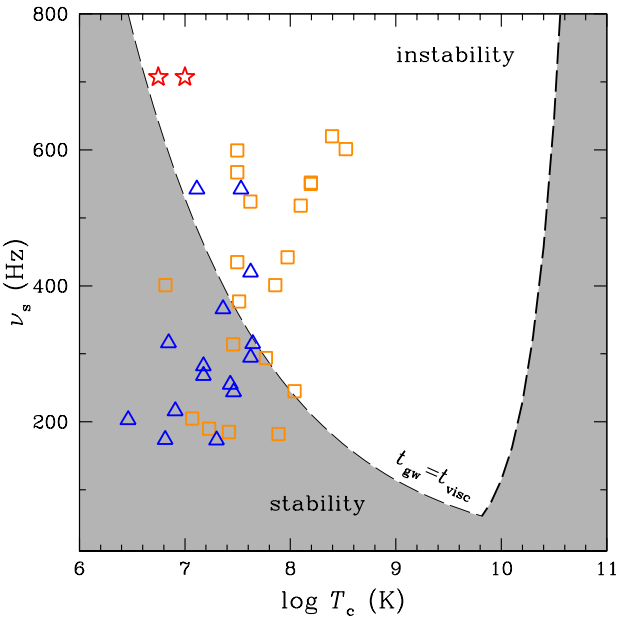

Figure 3. R-mode instability window. Neutron star core temperature T_c versus spin frequency ν_s. Dashed line denotes the boundary set by $t_{gw} = t_{visc}$, with the shaded "stability" region set by $t_{gw} > t_{visc}$ and r-mode is damped by viscosity and unshaded "instability" region set by $t_{gw} < t_{visc}$ and r-mode grows by emission of gravitational waves. Stars indicate (T_c,ν_s) for PSR J0952−0607, where the higher T_c is obtained from spectral fitting with variable N_H and lower T_c from fixed $N_H = 1 \times 10^{21}$ cm^{-2} (see text). Triangles and squares denote millisecond pulsars and neutron stars in a low-mass X-ray binary, respectively (see text).

illustrated in the left panel of Figure 4 (see Haskell et al. 2009, 2012, for details; see also Ho et al. 2011).

As noted above, PSR J0952−0607 is inside the traditional r-mode instability region shown in Figure 3. If the measured rate of change of spin frequency $\dot{\nu}_s$ is due (entirely) to energy loss by gravitational wave emission at a constant r-mode oscillation amplitude α, then the amplitude is

$$\alpha \approx 2 \times 10^{-8} \left(\frac{1000 \text{ Hz}}{\nu_s}\right)^{7/2} \left(\frac{\dot{\nu}_s}{10^{-15} \text{ Hz s}^{-1}}\right)^{1/2} \quad (5)$$

(Owen et al. 1998; Andersson & Kokkotas 2001) and is $\alpha = 1 \times 10^{-7}$ for PSR J0952−0607. Another constraint on α is set by the balance between viscous heating (by the aforementioned electron-electron scattering) of an unstable r-mode and cooling by surface radiation (at these low temperatures, surface photon emission dominates core neutrino emission). This yields

$$\alpha = 1.1 \times 10^{-9} \left(\frac{L_{th}}{10^{30} \text{ erg s}^{-1}}\right)^{1/2} \left(\frac{T_c}{10^7 \text{ K}}\right) \left(\frac{1000 \text{ Hz}}{\nu_s}\right)$$

$$\sim 3 \times 10^{-10} \left(\frac{L_{th}}{10^{30} \text{ erg s}^{-1}}\right)^{31/34} \left(\frac{1000 \text{ Hz}}{\nu_s}\right) \quad (6)$$

(Owen et al. 1998; Andersson & Kokkotas 2001), where L_{th} is thermal luminosity and the second equality makes use of equation (2). Alternatively, if we assume that PSR J0952−0607 lies on the boundary between stability and instability, such that $t_{gw} = t_{visc}$, then balance of heating and cooling yields

$$\alpha = 1.6 \times 10^{-10} \left(\frac{L_{th}}{10^{30} \text{ erg s}^{-1}}\right)^{1/2} \left(\frac{1000 \text{ Hz}}{\nu_s}\right)^{4} \quad (7)$$

(Mahmoodifar & Strohmayer 2013). Since we see from Figure 3 that PSR J0952−0607 is near the boundary, such that $t_{gw} \sim t_{visc}$, equations (6) and (7) give similar values of $\alpha \sim 1 \times 10^{-9}$. These constraints on r-mode amplitude are among the strongest obtained thus far. For example, X-ray observations yield upper limits of $\alpha \approx 10^{-8} - 10^{-6}$ for millisecond pulsars and neutron stars in a low-mass X-ray binary (Mahmoodifar & Strohmayer 2013; Chugunov et al. 2017; Mahmoodifar & Strohmayer 2017; Schwenzer et al. 2017) and of $\sim 2 \times 10^{-9}$ for the 542 Hz pulsar 47 Tucanae aa (Bhattacharya et al. 2017).

A phenomenological approach to constraining the shape of the r-mode instability window with observed millisecond pulsars and low mass X-ray binaries is suggested by Chugunov et al. (2017). They find observed systems require suppression of the instability in two extra regions: at $T_c \sim 10^8$ K and at 2×10^7 K $\lesssim T_c \lesssim 3 \times 10^7$ K (see light shaded regions in right panel of Figure 4). The first region is required for consistency with the hottest neutron stars in a low mass X-ray binary, while the second is needed for colder neutron stars in a low mass X-ray binary and upper limits on the surface temperature of millisecond pulsars. Extension of the second constraint to even lower temperatures (see hatched regions in right panel of Figure 4) may be needed due to surface temperature limits of 47 Tucanae aa (Bhattacharya et al. 2017) and PSR J0952−0607 presented here, such that the r-mode instability is not active at $T_c \lesssim 3 \times 10^7$ K, although isolated regions of instability are not excluded (see, e.g., Gusakov et al. 2014). Finally, Chugunov et al. (2017) argue that the r-mode instability can be almost unsuppressed at 7×10^7 K $\lesssim T_c \lesssim 10^8$ K while still remaining consistent with observations; in such a case, this leads to a class of rapidly rotating non-accreting neutron stars which are heated by the r-mode instability (see also Chugunov et al. 2014).

Gravitational waves from PSR J0952−0607 could be detectable if the r-mode amplitude $\alpha \gtrsim 1 \times 10^{-7} (h_0/h_{sd})$ or the pulsar has an ellipticity $\varepsilon \gtrsim 6.9 \times 10^{-10} (h_0/h_{sd})$,

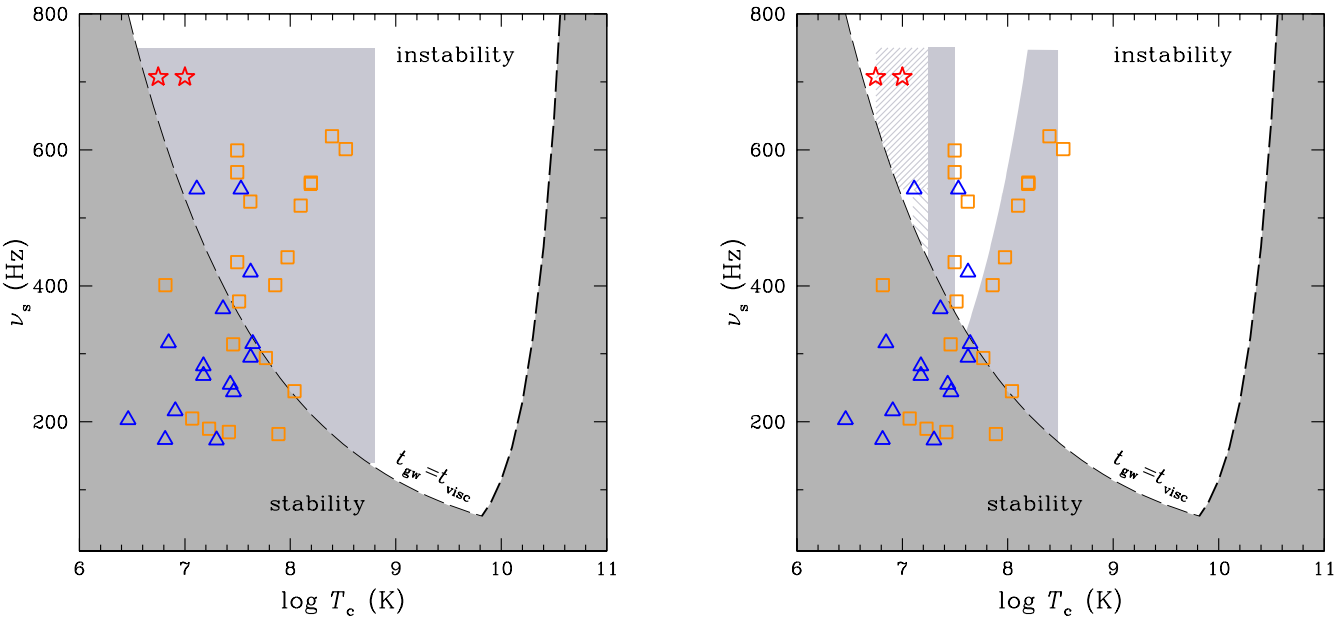

Figure 4. R-mode instability window. Neutron star core temperature T_c versus spin frequency ν_s. Dark shading denotes stability region due to shear viscosity by electron-electron scattering, and no shading denotes instability region. (T_c,ν_s) for PSR J0952−0607, millisecond pulsars, and neutron stars in a low-mass X-ray binary are denoted by stars, triangles, and squares, respectively. See Figure 3 caption for more details. Left panel: Light shading denotes stability region due to superfluid mutual friction. Right panel: Light shading and hatching denote regions required to stabilize r-modes in observed systems.

where h_0 is gravitational wave strain amplitude and h_{sd} is the "spin-down limit" amplitude obtained by assuming the pulsar's entire rotational energy loss is due to gravitational wave emission; note that h_0 and h_{sd} depend on frequency and gravitational wave mechanism (e.g., $h_{sd} \approx 8 \times 10^{-28}$ for an ellipticity in PSR J0952−0607). Gravitational wave searches of PSR J0952−0607 using LIGO 2015–2017 data are sensitive to $h_0/h_{sd} \sim 60$ and thus are not able to physically constrain ε (Abbott et al. 2019b; Nieder et al. 2019).

Finally, the observing mode of the *XMM-Newton* data presented here is not able to resolve pulsations at the 1.41 ms spin period of PSR J0952−0607. Detection of pulsations using *XMM-Newton* timing mode (with a time resolution of 0.03 ms) could permit discrimination between spectral models and determination of the size of the X-ray emitting region on the neutron star. Modeling of the pulse profile could even lead to some constraints on the nuclear equation of state (e.g., Bogdanov 2013), such as that being done with observations of other millisecond pulsars using *NICER* (Gendreau et al. 2012).

The authors thank the anonymous referee for useful comments. WCGH appreciates use of computer facilities at the Kavli Institute for Particle Astrophysics and Cosmology. WCGH acknowledges support through grants 80NSSC19K0668 from NASA and ST/R00045X/1 from the Science and Technology Facilities Council in the United Kingdom. COH is supported by NSERC Discovery Grant RGPIN-2016-04602 and a Discovery Accelerator Supplement. AIC acknowledges support by RFBR according to the research project 18-32-20170. This work is based on observations obtained with *XMM-Newton*, an ESA science mission with instruments and contributions directly funded by ESA Member States and NASA.

Facility: *XMM-Newton*

Software: CIAO 4.11 (Fruscione et al. 2006), SAS 17.0.0 (Gabriel et al. 2004), Xspec 12.10.1 (Arnaud 1996)

REFERENCES

Abbott, B. P., Abbott, R., Abbott, T. D., et al. 2017, PhRvD, 95, 082005

—. 2019a, ApJ, 875, 122

—. 2019b, ApJ, 879, 10

Alford, M. G., Mahmoodifar, S., & Schwenzer, K. 2012a, PhRvD, 85, 044051
—. 2012b, PhRvD, 85, 024007
Alpar, M. A., Anderson, P. W., Pines, D., & Shaham, J. 1984a, ApJ, 278, 791
Alpar, M. A., Pines, D., Anderson, P. W., & Shaham, J. 1984b, ApJ, 276, 325
Andersson, N. 1998, ApJ, 502, 708
Andersson, N., & Kokkotas, K. D. 2001, International Journal of Modern Physics D, 10, 381
Arnaud, K. A. 1996, in Astronomical Society of the Pacific Conference Series, Vol. 101, Astronomical Data Analysis Software and Systems V, ed. G. H. Jacoby & J. Barnes, 17
Backer, D. C., Kulkarni, S. R., Heiles, C., Davis, M. M., & Goss, W. M. 1982, Nature, 300, 615
Bassa, C. G., Pleunis, Z., Hessels, J. W. T., et al. 2017, ApJL, 846, L20
Becker, W. 2009, in Astrophysics and Space Science Library, Vol. 357, Astrophysics and Space Science Library, ed. W. Becker, 91
Bhattacharya, S., Heinke, C. O., Chugunov, A. I., et al. 2017, MNRAS, 472, 3706
Bogdanov, S. 2013, ApJ, 762, 96
Caride, S., Inta, R., Owen, B. J., & Rajbhand ari, B. 2019, arXiv e-prints, arXiv:1907.04946
Chakrabarty, D. 2008, in American Institute of Physics Conference Series, Vol. 1068, American Institute of Physics Conference Series, ed. R. Wijnands, D. Altamirano, P. Soleri, N. Degenaar, N. Rea, P. Casella, A. Patruno, & M. Linares, 67–74
Chakrabarty, D., Morgan, E. H., Muno, M. P., et al. 2003, Nature, 424, 42
Chandrasekhar, S. 1970, Physical Review Letters, 24, 611
Chugunov, A. I. 2017, PASA, 34, e046
Chugunov, A. I., Gusakov, M. E., & Kantor, E. M. 2014, MNRAS, 445, 385
—. 2017, MNRAS, 468, 291
Cook, G. B., Shapiro, S. L., & Teukolsky, S. A. 1994, ApJL, 423, L117
De Luca, A., Caraveo, P. A., Mereghetti, S., Negroni, M., & Bignami, G. F. 2005, ApJ, 623, 1051
Dickey, J. M., & Lockman, F. J. 1990, ARA&A, 28, 215
Forestell, L. M., Heinke, C. O., Cohn, H. N., et al. 2014, MNRAS, 441, 757
Friedman, J. L., & Morsink, S. M. 1998, ApJ, 502, 714
Friedman, J. L., & Schutz, B. F. 1978, ApJ, 222, 281
Fruscione, A., McDowell, J. C., Allen, G. E., et al. 2006, in Society of Photo-Optical Instrumentation Engineers (SPIE) Conference Series, Vol. 6270, 62701V
Gabriel, C., Denby, M., Fyfe, D. J., et al. 2004, in Astronomical Society of the Pacific Conference Series, Vol. 314, Astronomical Data Analysis Software and Systems (ADASS) XIII, ed. F. Ochsenbein, M. G. Allen, & D. Egret, 759
Gänsicke, B. T., Braje, T. M., & Romani, R. W. 2002, A&A, 386, 1001
Gendreau, K. C., Arzoumanian, Z., & Okajima, T. 2012, in Proc. SPIE, Vol. 8443, Space Telescopes and Instrumentation 2012: Ultraviolet to Gamma Ray, 844313
Gittins, F., & Andersson, N. 2019, MNRAS, 488, 99
Gonzalez-Caniulef, D., Guillot, S., & Reisenegger, A. 2019, arXiv e-prints, arXiv:1904.12114
Gudmundsson, E. H., Pethick, C. J., & Epstein, R. I. 1982, ApJL, 259, L19
Guillot, S., Kaspi, V. M., Archibald, R. F., et al. 2016, MNRAS, 463, 2612
Gusakov, M. E., Chugunov, A. I., & Kantor, E. M. 2014, PhRvD, 90, 063001
Gusakov, M. E., Kantor, E. M., & Reisenegger, A. 2015, MNRAS, 453, L36
Haensel, P., Lasota, J. P., & Zdunik, J. L. 1999, A&A, 344, 151
Haskell, B., Andersson, N., & Passamonti, A. 2009, MNRAS, 397, 1464
Haskell, B., Degenaar, N., & Ho, W. C. G. 2012, MNRAS, 424, 93
He, C., Ng, C.-Y., & Kaspi, V. M. 2013, ApJ, 768, 64
Heinke, C. O., Rybicki, G. B., Narayan, R., & Grindlay, J. E. 2006, ApJ, 644, 1090
Hessels, J. W. T., Ransom, S. M., Stairs, I. H., et al. 2006, Science, 311, 1901
Heyl, J. S. 2002, ApJL, 574, L57
Ho, W. C. G., Andersson, N., & Haskell, B. 2011, Physical Review Letters, 107, 101101
Ho, W. C. G., & Lai, D. 2001, MNRAS, 327, 1081
Kargaltsev, O., Durant, M., Pavlov, G. G., & Garmire, G. 2012, ApJS, 201, 37
Lee, J., Hui, C. Y., Takata, J., et al. 2018, ApJ, 864, 23
Levin, Y. 1999, ApJ, 517, 328
Mahmoodifar, S., & Strohmayer, T. 2013, ApJ, 773, 140
—. 2017, ApJ, 840, 94
Main, R., Yang, I. S., Chan, V., et al. 2018, Nature, 557, 522
Marelli, M., Mignani, R. P., De Luca, A., et al. 2015, ApJ, 802, 78
Meadors, G. D., Goetz, E., Riles, K., Creighton, T., & Robinet, F. 2017, PhRvD, 95, 042005
Nieder, L., Clark, C. J., Bassa, C. G., et al. 2019, arXiv e-prints, arXiv:1905.11352

Owen, B. J., Lindblom, L., Cutler, C., et al. 1998, PhRvD, 58, 084020

Papitto, A., Torres, D. F., Rea, N., & Tauris, T. M. 2014, A&A, 566, A64

Patruno, A., Haskell, B., & Andersson, N. 2017, ApJ, 850, 106

Petrovich, C., & Reisenegger, A. 2010, A&A, 521, A77

Potekhin, A. Y., Chabrier, G., & Yakovlev, D. G. 1997, A&A, 323, 415

Potekhin, A. Y., Pons, J. A., & Page, D. 2015, SSRv, 191, 239

Rangelov, B., Pavlov, G. G., Kargaltsev, O., et al. 2017, ApJ, 835, 264

Reisenegger, A. 1995, ApJ, 442, 749

Salvetti, D., Mignani, R. P., De Luca, A., et al. 2017, MNRAS, 470, 466

Schwenzer, K., Boztepe, T., Güver, T., & Vurgun, E. 2017, MNRAS, 466, 2560

Shternin, P. S., & Yakovlev, D. G. 2008, PhRvD, 78, 063006

Wilms, J., Allen, A., & McCray, R. 2000, ApJ, 542, 914